

Research Article

Estimating Snow Depth and Snow Water Equivalence Using Repeat-Pass Interferometric SAR in the Northern Piedmont Region of the Tianshan Mountains

Hui Li,¹ Zuo Wang,² Guangjun He,³ and Wang Man¹

¹Department of Spatial Information Science and Engineering, Xiamen University of Technology, Xiamen 361024, China

²College of Territorial Resources and Tourism, Anhui Normal University, Wuhu 241003, China

³State Key Laboratory of Space-Ground Integrated Information Technology, Space Star Technology Co. Ltd., China Academy of Space Technology, Beijing 100086, China

Correspondence should be addressed to Hui Li; lih666@xmut.edu.cn

Received 17 November 2016; Revised 6 February 2017; Accepted 6 March 2017; Published 12 April 2017

Academic Editor: Stephane Evoy

Copyright © 2017 Hui Li et al. This is an open access article distributed under the Creative Commons Attribution License, which permits unrestricted use, distribution, and reproduction in any medium, provided the original work is properly cited.

Snow depth and Snow Water Equivalence (SWE) are important parameters for hydrological applications. In this application, a theoretical method of snow depth estimation with repeat-pass InSAR measurements was proposed, and a preliminary sensitivity analysis of snow phase changes versus the incident angle and snow density was developed. Moreover, the snow density and incident angle parameters were analyzed and calibrated, and the local incident angle was used as a substitute for the satellite incident angle to improve the snow depth estimation. From the results, the coherence images showed that a high degree of coherence can be found for dry snow, and, apart from the effect of snow, land use/cover change due to a long temporal baseline and geometric distortion due to the rugged terrain were the main constraints for InSAR technique to measure snow depth and SWE in this area. The result of snow depth estimation between July 2008 and February 2009 demonstrated that the average snow depth was about 20 cm, which was consistent with the field survey results. The areal coverage of snow distribution estimated from the snow depth and SWE results was consistent with snow cover obtained from HJ-1A CCD optical data at the same time.

1. Introduction

Seasonal snow cover is one of the most important components in predicting global water- and energy-cycle consequences due to earth-system variability and change [1]. Snow depth is one of the most important parameters for hydrological applications and can dominate local and regional climate and hydrology. Snow Water Equivalence (SWE) represents the total amount of water available if the snowpack were melted instantaneously. Remote sensing is a powerful tool that offers the ability to examine quantitatively the physical properties of snow in remote or otherwise inaccessible areas where obtaining measurements may be expensive and dangerous [2]. Remote-sensing practitioners have strived for many years to measure snow depth and SWE from satellite-based sensors but have had limited success [3].

As opposed to optical sensors, active microwave sensors, especially Synthetic Aperture Radar (SAR), can be collected

at nighttime and through cloud cover [4]. SAR observations provide high-resolution measurements that are comparable to the scale of topographical variation in mountainous areas, and these measurements are more suitable for monitoring snow cover than data from passive microwave instruments [5, 6]. SAR backscattering from a snow-covered area depends on (1) sensor parameters, which include frequency, polarization, and viewing geometry, and (2) snowpack and ground parameters, which include snow density, liquid water content, particle size and shape of water and ice, and surface roughness parameters [7]. Snow depth estimation from SAR backscattering measurements requires very accurate inversion models and is a very complex process [8]. InSAR is the most notable application of spaceborne SAR for monitoring dynamic changes. It is achieved by using the repeat-pass pattern, in which two SAR images are acquired by the same antenna, and the area is revisited in a specific time interval.

During the past decades, spaceborne SAR interferometry has been successfully used to measure millimeter- to meter-level deformation on the surface due to earthquakes, landslides, glacier movements, and displacement on Earth's surface [9–11], and the data have been used extensively to map snow cover, temporal snowpack conditions, and snow evolution, perform coherence analysis, and estimate snow depth and SWE [12–17].

Radar backscattering from dry snow and that from a snow-free surface are similar in the C-band [18], because the penetration depth of InSAR signals can reach tens of meters in dry snow [19]. The ground beneath the snow rather than the snow crystals represents the major source of the backscattering signal [13, 14]. Refraction of the radar beam in the snow/air interface is caused by the presence of dry snowpack, and the index of refraction is related to the density and permittivity of the snow [20]. Therefore, there is a difference between radar propagation through the atmosphere and radar propagation through dry snow, and there is a phase shift between the two SAR acquisitions with and without snow. Hence, using this geometry and physical properties of the snowpack, a relationship between phase shift and snow mass can be derived, and this represents a direct method for estimating snow depth or relative changes in SWE [13, 14].

However, repeat-pass InSAR can only work under coherent conditions where a high correlation exists between the SAR signals for the SAR acquisition pair [21]. Using repeat-pass InSAR for snow applications has several limitations that influence InSAR processing and the results: temporal decorrelation, atmospheric effects, and geometric distortions. As for snow depth estimation in mountainous areas, estimates derived by InSAR technology are also subject to various other restrictions: decorrelation, frequency-dependent phase wrapping ambiguities, and complicated processing of repeat-pass interferograms with specialized software compared to passive microwave algorithms [15]. A snow-free surface preserves high coherence between the two SAR acquisitions while a snow-covered one does not [15]. Hence, snow cover results in a significant decorrelation between the two SAR acquisitions over areas with and without snow. Light snowfall or small changes in snow properties can also cause height errors in the DEM derived from glaciers or bare ground, even if a high degree of coherence exists [13]. Phase wrapping occurs for snow depth changes of 16.4 cm, which equals a SWE of 3.3 cm when the snow density is 0.2 g/cm^3 at 23° incident angle in the C-band, and hence delta-K InSAR processing for deriving SWE of dry snow is applied by multiplying the two delta-K images from summer and winter [22]. Additionally, snow stratigraphy is another factor that strongly affects the microwave radiative and scattering properties of snow [23–25]. Snow stratigraphy can lead to a variation of snow densities in the vertical direction; therefore, volume scattering of snowpack cannot be neglected. However, it is difficult to retrieve/estimate snow depth of a layered snowpack from the SAR signal because the details of the layered condition are unknown and the wave transmit path in snowpack cannot be identified [26]. In spite of these problems, using InSAR data for snow depth and

SWE estimation has proved to be one of the most promising techniques in theoretical research [1].

The Manas River Basin, in the Northern Piedmont region of the Tianshan Mountains in Xinjiang, is the fourth largest irrigated area in China. In this mountainous region, snowfall is a substantial part of the overall precipitation and provides freshwater to over a million people in the city of Urumqi, the capital of Xinjiang, China. Additionally, snowmelt is a major component of total annual stream flow and has a significant influence on the hydrologic cycle in this region. However, it is very difficult and dangerous to gather sufficient information regarding the snowpack in this area, because this area is not easily accessible in the winter. Moreover, the published literature regarding snow depth estimation using SAR observations is limited [27, 28].

Thus, this research aims to develop a process to estimate snow depth and SWE with repeat-pass InSAR measurements by using Envisat ASAR IMS data. Without any direct measurements of snow characteristics when the InSAR pairs pass by, snow characteristics of measured data and hydrological station data at a different winter time were analyzed. The InSAR process is optimized to obtain a clear interferogram and right phase left due to the difference in the two-way propagation of the radar wave in the snowpack relative to the air. A preliminary sensitivity analysis was developed, and the rate of changes of snow phase versus the incident angle and snow density was calculated to see how these two parameters influence the snow phase. Lastly, the snow density and incident angle parameters were calibrated, and the local incident angle was used as a substitute for the satellite incident angle of 23° to improve the final snow depth estimation. And SWE was also calculated by using the directly linear relationship between the differential phase shift due to propagation in the snowpack and SWE, under the nominal incident angle 23° of Envisat ASAR. Apart from the snow, the influences of both terrain distortion and land use/cover types could also contribute to considerable deterioration in the degree of coherence for the coherence images. It is shown that snow depth estimation result can provide more detailed information on snow than SWE estimation. And the result of snow depth estimation between July 2008 and February 2009 demonstrated that the average snow depth was about 20 cm, which was consistent with the field survey results. Despite limited ground measurement to infer snowpack condition and validate snow depth or SWE estimation results, the comparison between snow depth/SWE estimation and snow-covered area from HJ-1A CCD optical data can be the evidence to verify InSAR technique to be the promising method to obtain snow depth and SWE in a higher resolution.

2. Study Area and Materials

2.1. Study Area. The Manas River Basin is the largest inland river in the Northern Piedmont region of the Tianshan Mountains. It covers a latitudinal range between $43^\circ 20' \text{N}$ and $44^\circ 55' \text{N}$ and a longitudinal range between $85^\circ 00' \text{E}$ and $86^\circ 10' \text{E}$, and the size of the area is 5156 km^2 (Figure 1(a)). The elevation of the study area ranges from 743 m to 5152 m. Generally, winter precipitation (November to next March)

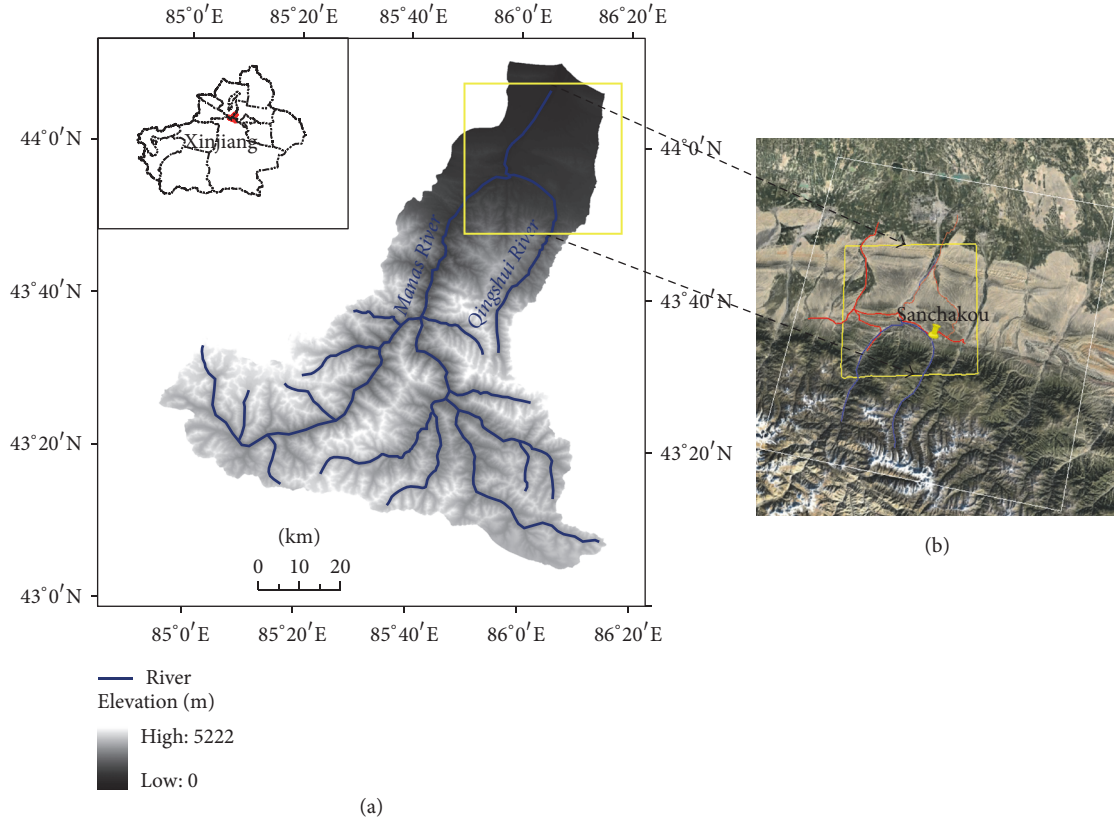


FIGURE 1: (a) The Manas River Basin is located in the north of Xinjiang, China, with two main rivers flowing through it: Manas and Qingshui River. (b) The white-bordered rectangle in the right picture shows the coverage of ASAR IMS images in our database, and the yellow one shows the demonstration area.

accumulates in the form of snow, especially at high elevation, and melts in summer (June to August), often leading to summer floods.

A pilot study was carried out for a $4\text{ km} \times 1.6\text{ km}$ demonstration area in the Manas River Basin (the yellow-bordered rectangle in Figure 1). The highest elevation in this area is 3422 m. This area has moderate topography. More than 78% of the area has slopes smaller than 20° . Less than 9% of the area has slopes greater than 30° . Thirteen percent of the area has slopes between 20° and 30° . The areas covered by the eight aspects (north, northeast, east, southeast, south, southwest, west, and northwest) are almost equal in size.

In terms of topographic mapping and deformation monitoring, ground truth may influence the quality of the correlation and even the final results, because the scattering properties of different types of land cover are various, and land cover/use change would occur during the time of InSAR pair acquisition. Therefore, the coherence of the InSAR pair is subject easily to land cover change, especially in the application of snow depth estimation by using repeat-pass InSAR measurement. Apart from a small amount of farmland along the river, the main area consists of mainly sparsely vegetated area (Figure 2). In areas above 2500 m, portions of the landscape exposed to the sun are mainly bare

TABLE 1: Temporal and spatial baseline of two InSAR pairs.

InSAR pair (master-slave)	080712-090103	090103-090207
Temporal baseline (days)	175	35
Perpendicular baseline (meters)	56.552	476.040
Critical baseline (meters)	934.975	934.891

land, whereas areas exposed to more shade are covered with coniferous forest (Figure 2).

2.2. Materials

2.2.1. Envisat ASAR IMS. The Envisat satellite is equipped with a C-band ASAR instrument. A set of slant-range complex ASAR IMS products are used for interferometric measurements with swath IS2 and a nominal incident angle range of 19.2° – 26.7° . Scenes acquired with the same frame 2720 and track 162 were chosen to generate an interferogram for the Manas River Basin. The overpass time was 04:33 a.m. local time for the study area in the descending orbits. The data in the following sections are renamed following the yymmdd format, denoting the time of data acquisition [28].

Two InSAR pairs, 090103-080712 and 090103-090207, were used in the snow depth and SWE estimation (Table 1).

TABLE 2: Snow parameters from field measurement in the Sanchakou site.

	Location	Local time (yyyymmdd)	Snow density (g/cm^3)	Permittivity		Snow depth range (cm)
				Real part	Imaginary part	
Sanchakou	43°55'53"N 86°12'33"E	20111207	0.14	1.34	0.009	7-8

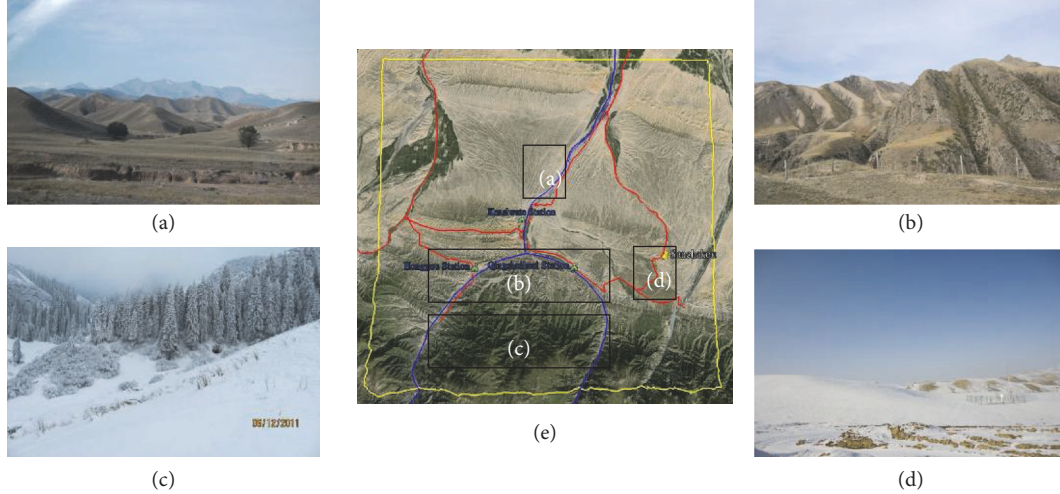


FIGURE 2: The study area consists of several typical kinds of land cover. There are (a) bare land with sparse grass in most areas without snow, (b) bare land exposed to the sun, (c) coniferous forest in the shade aspect, and (d) ground covered with snow and no grass in the winter. (c) shows an area in the Sanchakou site. (e) shows the study area with background from Google Earth.

There was no snow on 12 June 2008, and snow covered on 3 January 2009 and 7 February 2009. Therefore, the InSAR pair 090103-080712 represents the snow depth on 3 January 2009, and 090103-090207 depicts the snow depth change between 7 February 2009 and 3 January 2009.

2.2.2. Field Measurements Data. With regard to the snow-climate class, the snow type of the Tianshan Mountains area is dry and cold in the winter [29]. We measured snow parameters in Sanchakou automatic weather station, within the study area (see Figure 2). Table 2 lists the mean values of snow parameters including snow density, real and imaginary part of the snow permittivity, and snow depth, respectively. This was not the first snowfall in this region.

We also measured snow characters and environmental factors in three other sites, that is, Fukang (44°17'24"N, 87°55'50"E, 20101207), Dunde (43°15'4"N, 85°20'50"E, 20120411), and Aerxiangou (43°25'26"N, 84°42'2"E, 20120412), from the year of 2010 to 2012 and from December to next April. These sites were not within the study area, but all these sites were located in the central Tianshan Mountains. From December 2010 to April 2012, four field measurements were carried out to investigate the snow characteristics and their variation tendency in a snow season, using a snow fork, a portable instrument for measuring the properties of snow. A large number of snow pits were measured in detail, and the measurements included snow depth, grain size, density,

snow dielectric constant, snow temperature, temperature at both snow/ground and air/snow interfaces, and stratigraphy of the snowpack.

Although these measured data were obtained in different years, the data are assumed to represent the snow characteristics within a snow season in the central Tianshan Mountains. The mean snow density ranged from $0.14 \text{ g}/\text{cm}^3$ to $0.25 \text{ g}/\text{cm}^3$ from December to April of the following year. And, with the aging of snow, snow density increased and reached the peak (measured to be $0.25 \text{ g}/\text{cm}^3$) when snow was melting. Snow temperature varies with time of day. A snow temperature profile was obtained for a 24-hour period from 7 December 2011 to 8 December 2011, using a temperature logger located in the snowpack at 2-3 cm depth. And the temperature in snowpack was measured to be at -7°C stability for a long period from 10:00 p.m. to 10:00 a.m. the next day; therefore, it was assumed that the snow was in a dry condition due to the cold winter night. It is worth pointing out that the measurements were all carried out during the daytime, most of them at noon, whereas the satellite overpass occurred at 04:33 a.m. in the cold night. Therefore, it can be assumed that the temperature in the snowpack was below 0°C and the liquid water content was likely reduced to 0 when the SAR was passing by.

Despite limited ground measurements to infer snowpack conditions at the time of InSAR pair passing by, these measurement data showed a general change trend of snow

characters in a snow season. And it can be inferred that the snow should remain in a dry condition in the study area during January and February.

2.2.3. Air Temperature Data from the Hydrological Station. Air temperature data were obtained from the Kensiwater hydrological station, the control station at the confluence of Manas main streams and tributaries, at an elevation of 910 m and a control area of 4637 km². Figure 3 shows the station's monthly maximum, minimum, and average air temperatures in the years of 2002 and 2004. Air temperatures in January, February, March, November, and December were all below 0°C, and minimum temperatures usually occurred in January and February. With regard to the snow season, snowmelt can be considered to take place in late March or early April, which coincided with the field measurements. Note that the maximum air temperature in December was above 0°C, which is a factor that cannot be ignored because it leads to snow in the cycles of freezing and thawing.

2.2.4. Snow Depth Survey Data. Seven snow observation sites were used to obtain snow depth data from the Shihezi Hydrology and Water Resources Survey Bureau. All these sites were located in mountainous areas below the elevation of 1600 m. Since 1998, snow depth data have been collected on the last day of each month from November to next March. Results indicated that, in general, the maximum value of snow depth occurred in the last days of February, the highest snow depth record was 53 cm, and the average snow depth was about 20–28 cm [28]. And no field measurements were obtained in subalpine or alpine areas above 1600 m which were not accessible due to rugged terrain.

3. Methodology

3.1. Theory

3.1.1. InSAR and DInSAR Theory. On the basis of the theories repeat-pass InSAR and DInSAR, the observed phase values ϕ_1 and ϕ_2 in the two images for a resolution point are

$$\begin{aligned}\phi_1 &= \frac{4\pi}{\lambda}R + n_1, \\ \phi_2 &= \frac{4\pi}{\lambda}(R + \Delta R) + n_2,\end{aligned}\quad (1)$$

where R and $R + \Delta R$ are the radar range distances, λ is the radar wavelength, and n_1 and n_2 are the contributions of the scattering phases in both images.

If the scattering characteristics are equal during acquisition (i.e., $n_1 = n_2$), mathematically, the interferometric phase ϕ can be extracted by

$$\phi = \phi_1 - \phi_2 = -\frac{4\pi}{\lambda}\Delta R + (n_1 - n_2) = -\frac{4\pi}{\lambda}\Delta R, \quad (2)$$

where ΔR is the one-way range difference. The equation shows that the interferometric phase is proportional to the

two-way range difference ΔR , which can be approximated as [30]

$$\Delta R \approx B \sin(\theta - \alpha) = B_{//}, \quad (3)$$

where B is the length of the baseline vector connecting two sensors and $B_{//}$ is the baseline component parallel to the radar look vector.

If there are changes during image acquisition times, interferometric phase will record any displacement of the ground along the radar line of sight that has occurred during the time interval between the two images. And the range difference is approximated as

$$\Delta R = \Delta R_0 + \delta d = B_{//} + \delta d. \quad (4)$$

Using (2), the interferometric phase is

$$\phi = \frac{4\pi}{\lambda}\Delta R = -\frac{4\pi}{\lambda}(B_{//} + \delta d). \quad (5)$$

Subtracting the phase caused by flat earth and by topography, the residual phase $\Delta\phi$, which may result not only from deformation, but also from changes in electromagnetic properties along the propagation path, is derived as follows:

$$\Delta\phi = \phi - \phi_0 = \frac{4\pi}{\lambda}\delta d, \quad (6)$$

where δd is the displacement in the radar line of sight (radar LOS).

3.1.2. InSAR for SWE/Snow Depth Estimation. In homogeneously dry snow, the main backscattering effect is due to the snow-ground interface (part (2) in Figure 4(b)), whereas the volume scattering is small and its effect on the interferometric phase is negligible (part (3) in Figure 4(b)) [13]. Thus, the radar wave refraction is presumably due to the difference in the dielectric properties changes of the propagation path of the radar beam vector, which occurs in the snow/air interface (Figure 4(b)) and therefore results in a phase shift.

Figure 4(a) illustrates the difference of the propagation path of radar waves with and without snow. For a nonmoving pixel, the radar wave range is shown as ΔR_s without snow cover, and $\Delta R_a + \Delta R_r$ is shown with snow due to the refraction of the radar beam in the snow-air interface. The range difference is represented by

$$\Delta R = \Delta R_s - (\Delta R_a + \Delta R_r). \quad (7)$$

For any kind of dry snow (fresh, old, or wind-pressed snow, depth hoar, and refrozen crusts), the permittivity ϵ_s of dry snow is a function of snow density ρ only. The relationship can be represented by $\epsilon_s = 1 + 1.6\rho + 1.86\rho^3$, and the refraction index, n , is $\epsilon_s = n^2$ [20].

According to (6) and (7), the snow phase ϕ_{snow} represents the difference in the two-way propagation with and without snow and can be derived as [13, 14]

$$\begin{aligned}\phi_{\text{snow}} &= -\frac{4\pi}{\lambda}d_s \left(\cos\theta_i - \sqrt{\epsilon_s - \sin^2\theta_i} \right) \\ &= -\frac{4\pi}{\lambda}d_s \left(\cos\theta_i - \sqrt{1 + 1.6\rho + 1.86\rho^3 - \sin^2\theta_i} \right),\end{aligned}\quad (8)$$

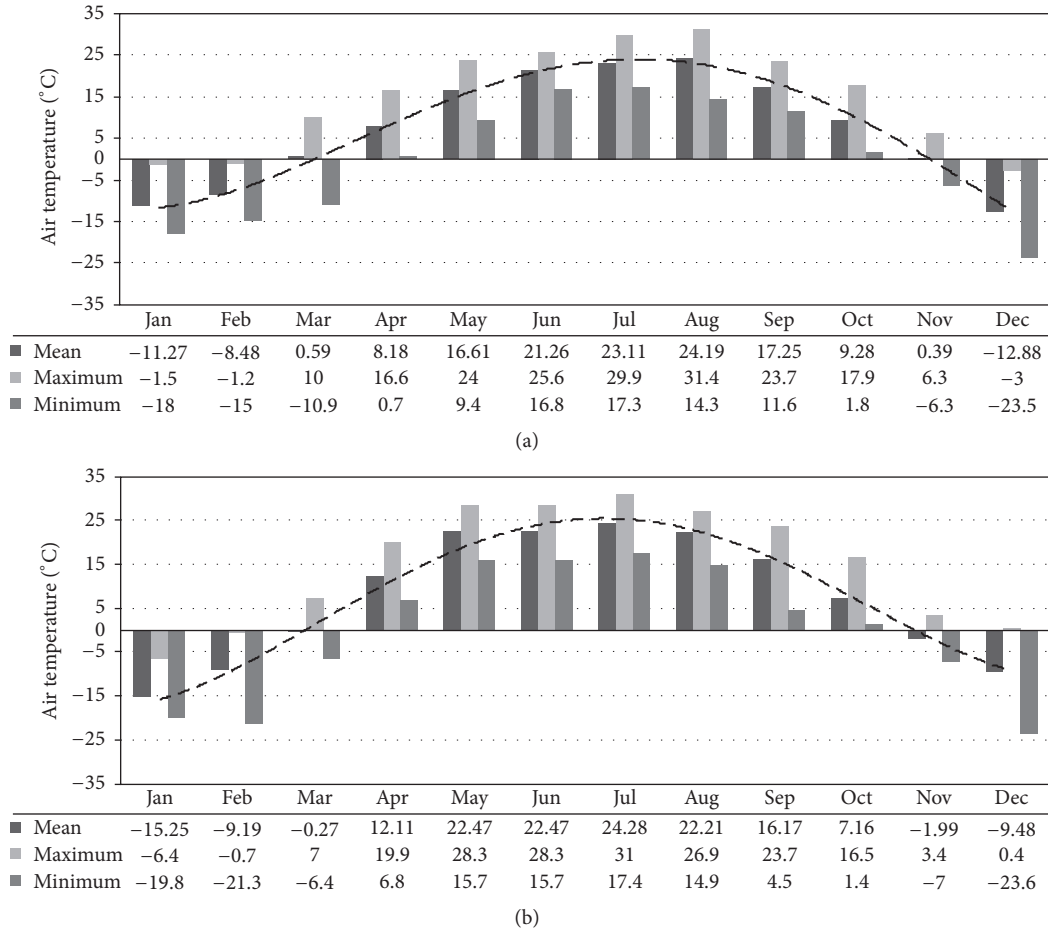


FIGURE 3: Air temperature data from the Kensiwate hydrological station in (a) 2002 and (b) 2004. The lowest temperature occurred in December, and air temperatures were above 0°C in April.

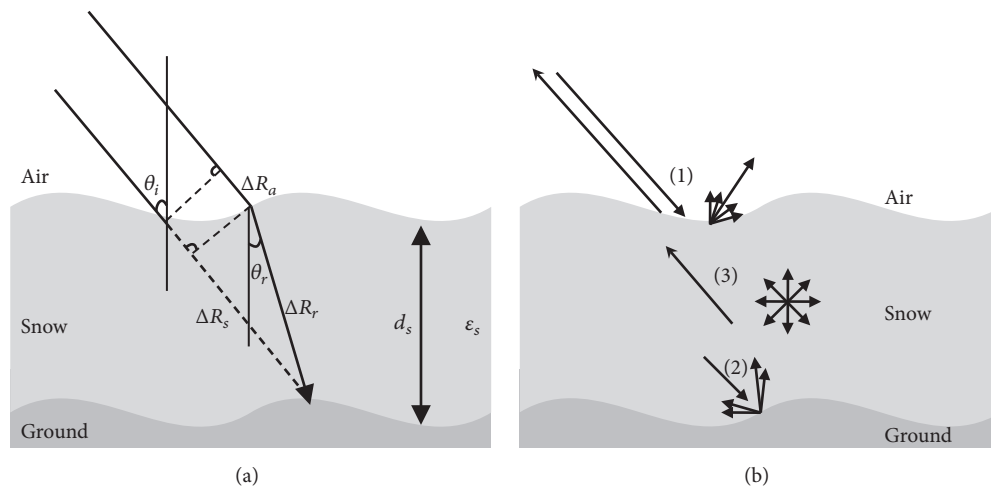


FIGURE 4: (a) Geometry of radar wave in snow and (b) scattering mechanism in snowpack (surface scattering in air-snow and snow-ground interface; volume scattering at snow grains within snowpack); (1) surface scattering at air-snow interface; (2) surface scattering at the ground-snow interface; (3) volume scattering at snow grains within the snowpack [17].

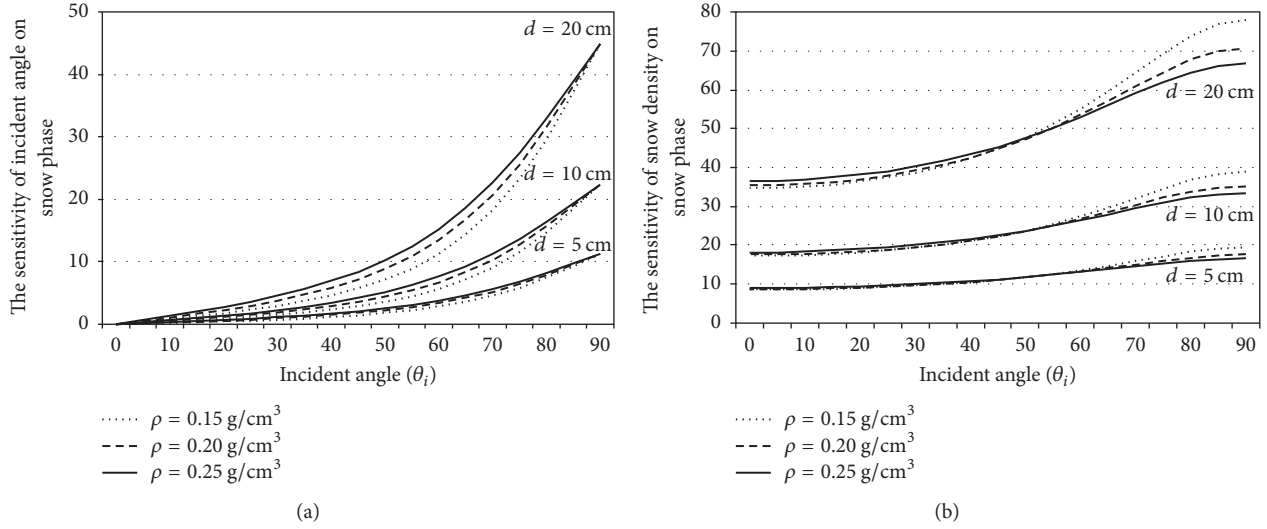


FIGURE 5: The sensitivity of (a) incident angle and (b) snow density on snow phase with snow densities $\rho = 0.15 \text{ g/cm}^3$, 0.20 g/cm^3 , and 0.25 g/cm^3 ; snow depths $d = 5 \text{ cm}$, 10 cm , and 20 cm .

where d_s is the depth of the snowpack; ϵ_s is dielectric constant of snow; λ is radar wavelength; θ_i is the incident angle.

And SWE, the mass of snow on ground, is the amount of water that can be obtained when a snowpack is completely melted. It can be represented by

$$\text{SWE} = \langle \rho \rangle d_s, \quad (9)$$

where $\langle \rho \rangle$ is the mean value of snow density in the snowpack.

For snow density ρ_s in a range of $0\text{--}0.5 \text{ g/cm}^3$, a linear approximation relation between the interferometric phase difference and SWE can be obtained by using $\theta_i = 23^\circ$, the nominal Envisat ASAR incident angle [13, 14]:

$$\Delta\phi_{\text{snow}} = -\frac{4\pi}{\lambda} 0.87 \Delta\text{SWE}. \quad (10)$$

Equation (10) demonstrates that there is a linear approximation between the InSAR phase difference of dry snow, $\Delta\phi_{\text{snow}}$, and changes in SWE. And also, according to (8) and (10), the InSAR phase difference of dry snow is a more accurate function of snow depth, with two parameters: incident angle θ_i and snow density ρ . Therefore, a preliminary sensitivity analysis was developed to see how these two parameters, incident angle θ_i and snow density ρ , would influence the phase difference obtained from InSAR measurement in the dry snow.

Based on the law of error propagation, according to (8), the sensitivities of incident angle θ_i and snow density ρ on

snow phase term ϕ_{snow} can be derived by taking the partial derivatives:

$$\frac{\partial\phi_{\text{snow}}}{\partial\theta_i} = -\frac{4\pi}{\lambda} \cdot d_s \left(-\sin\theta_i + \frac{\sin\theta_i \cos\theta_i}{\sqrt{1 + 1.6\rho + 1.86\rho^3 - \sin^2\theta_i}} \right) \quad (11)$$

$$\frac{\partial\phi_{\text{snow}}}{\partial\rho} = \frac{4\pi}{\lambda} d_s \frac{0.8 + 2.79\rho^2}{\sqrt{1 + 1.6\rho + 1.86\rho^3 - \sin^2\theta_i}}. \quad (12)$$

In the preliminary sensitivity analysis, several combinations of these parameters were verified in (11) and (12). From the field measurement data, the mean snow density was in the range of 0.14 g/cm^3 and 0.25 g/cm^3 in a snow season (from December to April of the following year) in the central Tianshan Mountains. And each spaceborne sensor platform has a different incident angle. In this application, Envisat ASAR IMS data were utilized with a nominal incident angle range of $19.2^\circ\text{--}26.7^\circ$. And also RADARSAT-1 and RADARSAT-2, with a range of 3–100 m in pixel size and incident angles of $20^\circ\text{--}49^\circ$, are satellite data sources frequently used in InSAR measurement. As may be noted from (8), the incident angle plays a very important role in the relationship of phase differences InSAR data and snow depth estimation. Previous research also concluded that the incident angle of sensors has a crucial influence on InSAR phase and also on SWE estimation [31].

Figure 5 depicts the rate of changes of snow phase versus the incident angle and snow density and reflects the sensitivity of the incident angle and snow density on snow phase (see (11) and (12)). Using the range of snow density ρ

available from field measurements data, the rates of variations of snow phase with respect to incident angle ranging from 0° to 90° were calculated (see (11) and (12)). Figure 5(a) demonstrates the fluctuation of the rate of snow phase change relative to the incident angle (see (11)). The three different kinds of curves (the dotted line, dashed line, and solid line) in Figure 5(a) show that the rates of changes, in different snow densities and with the same snow depth, are almost the same in snow depth $d = 5$ cm, while they are a little different in $d = 20$ cm, especially in the range of incident angle 25° – 75° . And all the curves in Figure 5(a) show that the rate of snow phase change increases exponentially with the increase of incident angle and rises dramatically with deeper snow ($d = 20$ cm). Figure 5(b) demonstrates the fluctuation of the rate of snow phase change with respect to the snow density (see (12)). The dotted line, dashed line, and solid line in Figure 5(b) demonstrate that the rates of snow phase change in three different snow densities are almost the same in the same snow depth $d = 5$ cm, while the differences in the rates of changes are enlarged when snow depth increases. And it can be figured out that the slopes of snow phase change are the same with the same snow depth and different snow densities in the incident angle 50° . In both Figures 5(a) and 5(b), an incident angle less than 50° does not show a significant effect on the rate of snow phase change with respect to the incident angle and snow density, but the snow phase increases exponentially for greater incident angles.

Given that coherence exists between the two SAR acquisitions with a coincidence of snowfall or redistribution, the total repeat-pass interferometric phase ϕ consists of the following contributions:

$$\phi = \phi_{\text{flat}} + \phi_{\text{topo}} + \phi_{\text{snow}} + \phi_{\text{atm}} + \phi_{\text{noise}}, \quad (13)$$

where ϕ_{flat} and ϕ_{topo} are the phase differences due to changes of the relative distance between satellite and target for flat earth and for topography, respectively. ϕ_{atm} results from changes in atmospheric propagation (heterogeneous atmospheric (ionosphere and (or) troposphere)), and ϕ_{noise} is phase noise. ϕ_{snow} is the two-way propagation difference in the snowpack relative to air and results from the refraction of the radar wave in dry snowpack (see (8)). The phase becomes meaningful and valuable when these components are separated from each other. Therefore, ϕ_{snow} would remain to estimate the snow depth and SWE after ϕ_{flat} , ϕ_{topo} , and ϕ_{atm} have been removed.

3.2. InSAR Processing Chain. All interferometric processing was performed using Gamma software developed by a Switzerland based company. The Gamma interferometry SAR processor (ISP) and Differential Interferometry and Geocoding (DIFF&GEO) encompass a full range of algorithms required for generation of interferograms, coherence maps, intensity images, and unwrapped phase and differential interferometric products. To remove “flat-earth” effect (ϕ_{flat} in (13)) in the interferometric results, the precise satellite position must be known during each acquisition. In this regard, the perpendicular baseline is defined as the perpendicular distance relative to the radar LOS of the satellite’s position

between each acquisition, and it is determined by extracting state vectors from Envisat ASAR DORIS precision orbit state vector files. For DInSAR system, the topographic phase (ϕ_{topo} in (13)) was simulated and geocoded using the external SRTM DEM, which was subtracted from the wrapped phase. The linear unflattened phase was simulated by the baseline model and removed completely after the baseline was refined [28].

And it is worth noting that ϕ_{atm} may be the principal sources of observed residual phase mixed in the snow phase ϕ_{snow} [32]. Accurate correction of the atmospheric phase screen in single InSAR pairs requires spatially detailed information on the atmospheric propagation conditions (in particular water vapor) which is usually not available [14]. Because this method works only for dry snow, atmospheric temperatures and water vapor content should be rather low, and therefore both the troposphere and the ionosphere effects may be considered negligible for cold winter months with low humidity at C-band [15]. Manas River Basin is a typical high-cold region, and both the troposphere and the ionosphere effects may be considered negligible in the winter. However, in the summer, in July, the atmosphere effects cannot be referred to in the SAR image 080712, without any detailed ground measurement data. Therefore, only the height-dependent atmospheric phase was removed after removal of the topographic and flattened phases.

Moreover, some steps in InSAR processing were optimized to guarantee a good interferogram [28]. The standard deviation of the InSAR pair’s fine registration was strictly controlled to remain below 0.1 pixels. From (8), phase wrapping occurs for a change in snow depth of 2.9 times the wavelength for a snow density of 0.2 g/cm^3 . Previous research concluded that C-band phase wrapping at an incident angle of 49° occurs at approximately 100 cm snow depth for a snow density of 0.3 g/cm^3 [31] and at every 49.2 mm of SWE at an incident angle of 23° [13]. And, in this application, phase wrapping does not occur due to a low snow density (the mean snow density of 0.18 g/cm^3) and a shallow snow depth (the snow depth less than 12 cm). Even though phase wrapping would not occur theoretically, phase unwrapping of the filtered differential interferogram is processed using the minimum cost flow (MCF) techniques and a triangular irregular network (TIN) in the Gamma software. The phase was unwrapped after the removal of the topographic and flattened phases, which can enhance the stability of the phase unwrapped results and reduce the error in alpine areas. The phase unwrapped results were interpolated to obtain a successive phase.

After all phase components were separated and removed, the remaining phase is assumed to be the snow phase (ϕ_{snow} in (13)) due to snow cover. Based on the geometric relationships between snow phase and snow depth, snow depth can be calculated using (8) by carrying the dielectric constant of snow ϵ_s (depending only on snow density ρ) and the incident angle θ_i [28].

3.3. Parameters Calibration. As shown in (8) and (10), snow depth and SWE can be estimated using InSAR measurements based on the hypotheses that the snow layer is uniform and

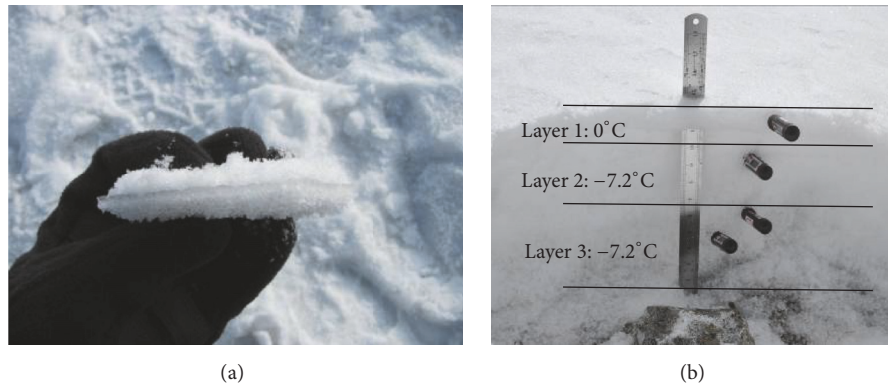
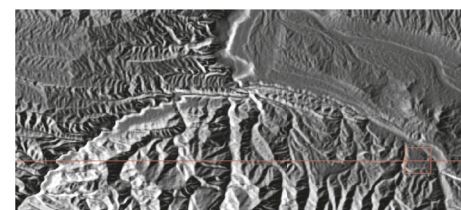


FIGURE 6: (a) Ice occurred in snow layers in Sanchakou site on 2011/12/07; (b) snow temperature measured in a layered snowpack on 2012/04/11. The top of the layer was 0°C due to a high air temperature, and, at the bottom of the snowpack, the crystallization was markedly different.

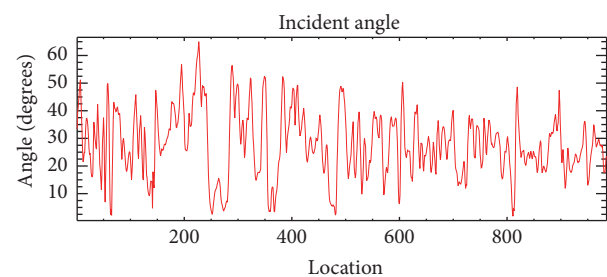
volume scattering within the snowpack is negligible [33]. Snow density ρ and incident angle θ_i are two crucial factors for snow depth estimation, as described previously. For a fixed SAR sensor platform, many theoretical studies in the InSAR measurement are based on using the satellite incident angle, such as the nominal 23° for Envisat ASAR, and a mean value of snow density. However, snow density varies as snow layers occur hierarchically in the natural environment, and the incident angle varies in the range of 19.2° – 26.7° for Envisat ASAR data [34].

Dry snow is a layered medium which is composed mostly of ice crystals and air. Snow metamorphism often occurs with the variation of a temperature gradient. These variations are complex and are affected by other factors, such as new snowfall and snow redistribution due to wind or gravity [28, 34]. Figure 6(a) shows that an ice layer was observed between the snow layers on 2011/12/07 in Sanchakou station (within the study area; see Figure 2). It was the second snowfall in this area occurring only after a few days of the first one. The freeze/thaw cycle may be the other reason for the layering, because the air temperature was measured at 6°C at noon. A vertical temperature gradient almost always exists in a snowpack due to high air temperature changes at the surface. Therefore, snow density should vary as snow hierarchy over the whole study area. And it is complicated and difficult to identify due to limited snow density ground measurements. Consequently, in this research, snow density is assumed to be equal to the mean value 0.18 g/cm^3 over the snowpack for snow depth estimation [28].

Envisat has a nominal incident angle fixed at 23° . Many previous theoretical studies in the InSAR application on snow depth and SWE estimation are based on this angle [13–15]. Using (8) for snow depth estimation, it was determined that the incident angle did not have a significant effect on phase delay, especially at values smaller than 30° . However, the phase difference increases exponentially for greater incident angles [31]. On the other hand, for SWE estimation, the phase difference has a linear relationship with the changes



(a)



(b)

FIGURE 7: (a) Profile line in local incident angle image through a rugged area; (b) depicts the fluctuation of the incident angle between 0° and 60° due to drastic local terrain changes along the profile line.

in SWE for different incident angles, and the SWE increases significantly with the incident angle. And, in the preliminary sensitivity analysis, incident angle indeed plays a very important role in InSAR phase differences, and an incident angle less than 50° does not show a significant effect on the rate of snow phase change, but the snow phase increases exponentially for greater incident angles. For ASAR mode IS2, the satellite incident angle ranges from 19.2° to 26.7° . The incident angle of the data in this research is 22.76° based on the header file. However, the incident angle varies over the whole study area because of the rugged terrain. The curve in Figure 7(b) shows the variation of incident angle of 0° – 60° due to the rugged terrain. The peak data of 60° occurred in a scarp near a valley.

4. Results

4.1. Interpretation of Results. There are three main results: (1) the coherence image of each pair, (2) the interferogram, fringe image, or relative change in the phase of each pair, and (3) estimation of snow depth for each pair. In general, the coherence image is a measure of consistency of scattering properties on the ground between the two SAR acquisitions, and also it can be used as a measure of the accuracy of the interferometric phase [21, 28]. In addition, as a measure of the similarity of the dielectric properties of the same pixel in an InSAR pair, the coherence analysis can be used for image classification [12], which has been applied in wet snow cover mapping [35, 36].

The absolute value of the coherence ranged between 0 and 1, where 1 stands for a complete correlation and 0 means no correlation. Figures 8(a) and 8(b) illustrate the coherence images of the 080712-090103 pair and the 090103-090207 pair. The coherence of the 090103-090207 pair is better than that of the 080712-090103 pair. The 080712-090103 pair has a 175-day time interval, much larger than the 090103-090207 pair. The coherence is affected mainly by a long temporal baseline, over which physical changes of the ground surface could occur. In addition, in July, the ground cover consisted of sparse grass and farmland near the river (see the green and red rectangular frames in Figures 8(a) and 8(b)) but was covered subsequently with snow in winter. As for the 090103-090207 pair, the area was mostly covered with snow, and then a high degree of coherence was found for dry snow. And the shorter distance of the perpendicular baseline of the 080712-090103 pair would imply that the calculated phase difference was affected less by topography and that the removal of these effects resulted in less change of the residual baseline.

In order to demonstrate the influence of topography on the coherence, two profiles were acquired to show the fluctuation in the degree of coherence (Figure 8). It can be seen that the altitude of profile 2 was generally higher than that of profile 1, and the local topographic relief of profile 2 was more dramatic (see Figures 8(g) and 8(h)). Even better coherence can be found in lower altitude (see profile 1 in Figure 8, mostly above 0.6) in both 080712-090103 pair and 090103-090207 pair; the coherence in higher altitude (see profile 2 in Figure 8) was less than 0.5. The coherence degree of profile 2 was stable and fluctuated between 0 and 0.5 (see Figures 8(c) and 8(f)), with a concentration of 0.2. The rugged terrain was the main reason for the low coherence or even decorrelation. According to Google Earth images and field surveys, the two locations that had a significant difference between the two pairs (shown in the red and green rectangles) were identified as farmland and covered with vegetation in the summer (see Figures 8(c) and 8(d)). In addition, the coniferous forest in the mountain areas also contributed to the decorrelation in profile 2, especially at a short wavelength C-band.

Image segmentation using the histogram threshold method (threshold is set to 0.5) was applied to the coherence images (Figure 9). The edges in the image of the 080712-090103 pair were coincident with the borders of farmland, but nothing similar was observed in the 090103-090207 pair.

The reason was a land use change from vegetation to snow between July 2008 and January 2009. Between January 2009 and February 2009, the land use type did not change, and only snowfall or redistribution occurred.

The relationship between surface movements and InSAR detected displacement in LOS direction is linearly proportional in valley regions with flat terrain [37]. And, for visualization purposes, the radar-LOS displacement maps of both InSAR pairs (Figures 10(a) and 10(b)) are shown to demonstrate the spatial distribution of the snow depth estimation results, because the displacement is linearly proportional to the SWE [15]. The estimation result of the 080712-090103 pair is assumed to be equivalent to the snow depth due to snowfall, because snow was nonexistent in July in this area. Therefore, the estimation result of the 090103-090207 pair is interpreted as change in snow depth between the two SAR acquisitions.

In a comparison with snow cover estimated from HJ-1A remotely sensed satellite imageries (dates: 2009/01/03 and 2009/02/09), it was evident that our estimation results of snow depth and SWE (the colored areas in Figures 10(a) and 10(b)) were similar to the snow distribution in the optical images (see Figures 10(c) and 10(d)), except for the areas undetected due to low coherence (Figures 8(a) and 8(b)). Thus, InSAR technology has the potential to identify the spatial patterns of snow depth/SWE and their changes and map snow cover under the condition of high coherence.

As described previously, typical densities of homogeneous snow and metamorphic winter snow in the study area ranged between 0.16 g/cm^3 and 0.25 g/cm^3 . The highest density of 0.25 g/cm^3 only occurred at the beginning of the snowmelt. An empirical value of 0.18 g/cm^3 for dry snow density was used to derive snow depth and SWE, and the local incident angle was used as a substitute for the satellite incident angle of 23° to improve the snow depth results. Figures 11(a) and 11(b) show the snow depth estimation result in 080712-090103 pair and snow depth change estimation result in 090103-090207 pair by using (8). Figures 11(c) and 11(d) show the SWE estimation result in 080712-090103 pair and SWE change estimation result in 090103-090207 pair by using (10). The snow depth and SWE estimation results (see Figure 11) can be considered reliable because the coherence degrees were all above 0.5, except for the dark blue colored area (see the red rectangle frame of Figures 11(b) and 11(d)). The snow depth and SWE estimation results of two InSAR pairs indicate that (1) the amount of snow depth (mainly caused by snowfall) in the 080712-090103 pair was greater than snow depth changes (snowfall or snow redistribution) in the 090103-090207 pair and (2) the average of snow depth was approximately 20 cm in February 2009, according to the statistics of the sum of 080712-090103 and 090103-090207 pairs, which was consistent with field survey results (in Section 2.2). Although there were limited detailed field measured data to validate the snow depth and SWE estimation, accordingly, snow depth results provide more details than SWE results due to a higher accuracy incident angle (see (8)) than the fixed 23° (see (10)). Compared with the HJ-1A CCD optical data (see Figures 10(c) and 10(d)), most of the snow-covered areas were detected. And, due

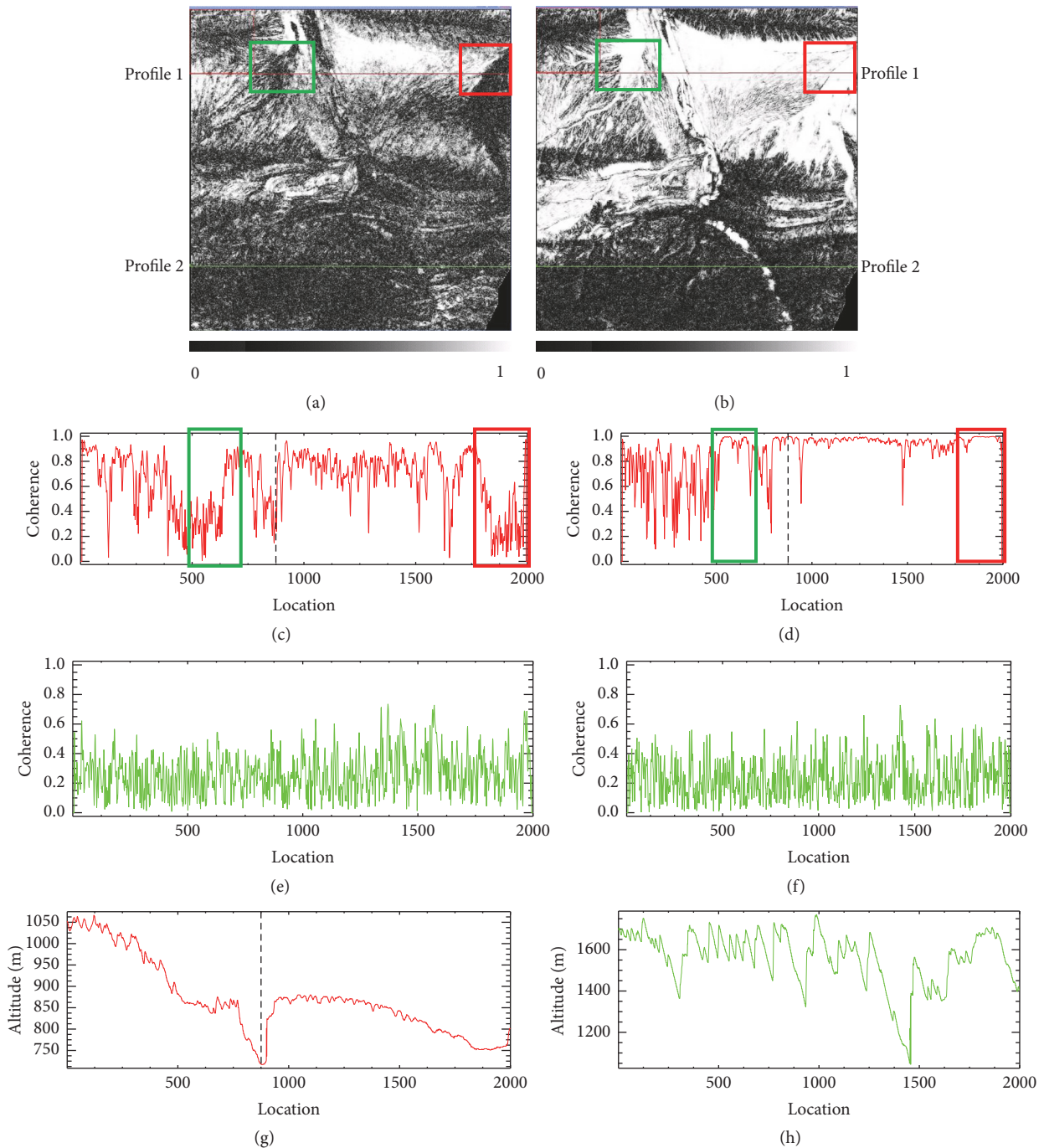


FIGURE 8: Profile 1 in red located in the Piedmont area and profile 2 in green in the mountain area for both (a) 080712-090103 and (b) 090103-090207 pairs. (g) and (f) demonstrate the variation of altitude of the two profiles. (c) and (e) show variations of coherence of the 080712-090103 pair of the two profiles, and (d) and (f) show those for the 090103-090207 pair. The vertical dashes in (c) and (g) represent the intersection of river valley and profile 1 and the lowest altitude, less than 750 m. Compared to the coherence of the two profiles in each pair ((c) and (e), (d) and (f)), the coherence degree of profile 1 in both InSAR pairs is much greater than of profile 2. (c) and (d) identify the two places in red and green rectangles as farmland, which have influences on decorrelation in the 080712-090103 pair, but not in the 090103-090207 pair.

to the lower coherence degree, the snow-covered areas in the 080712-090103 pair were recognized less than in the 090103-090207 pair. Despite limited ground measurement to infer snowpack condition and validate snow depth or

SWE estimation, the comparison between snow depth/SWE estimation and snow-covered area from optical images can be the evidence to verify the promising method to obtain snow depth and SWE in a higher resolution.

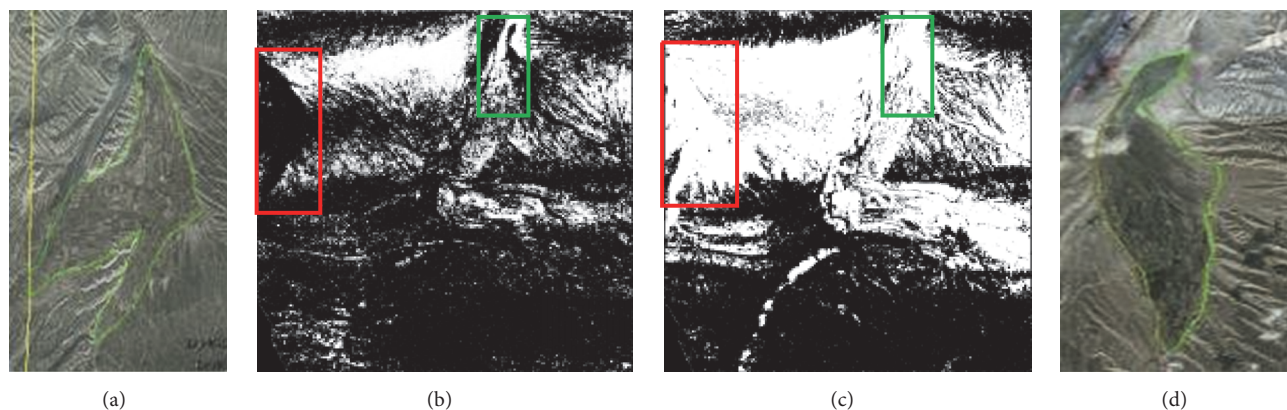


FIGURE 9: Segmentation results of coherence images using the histogram threshold method are shown for two farmland areas in (b) 080712-090103 obviously, but not in (c) 090103-090207. The borders of the farmland in (a) and (d) are consistent with the area of decorrelation.

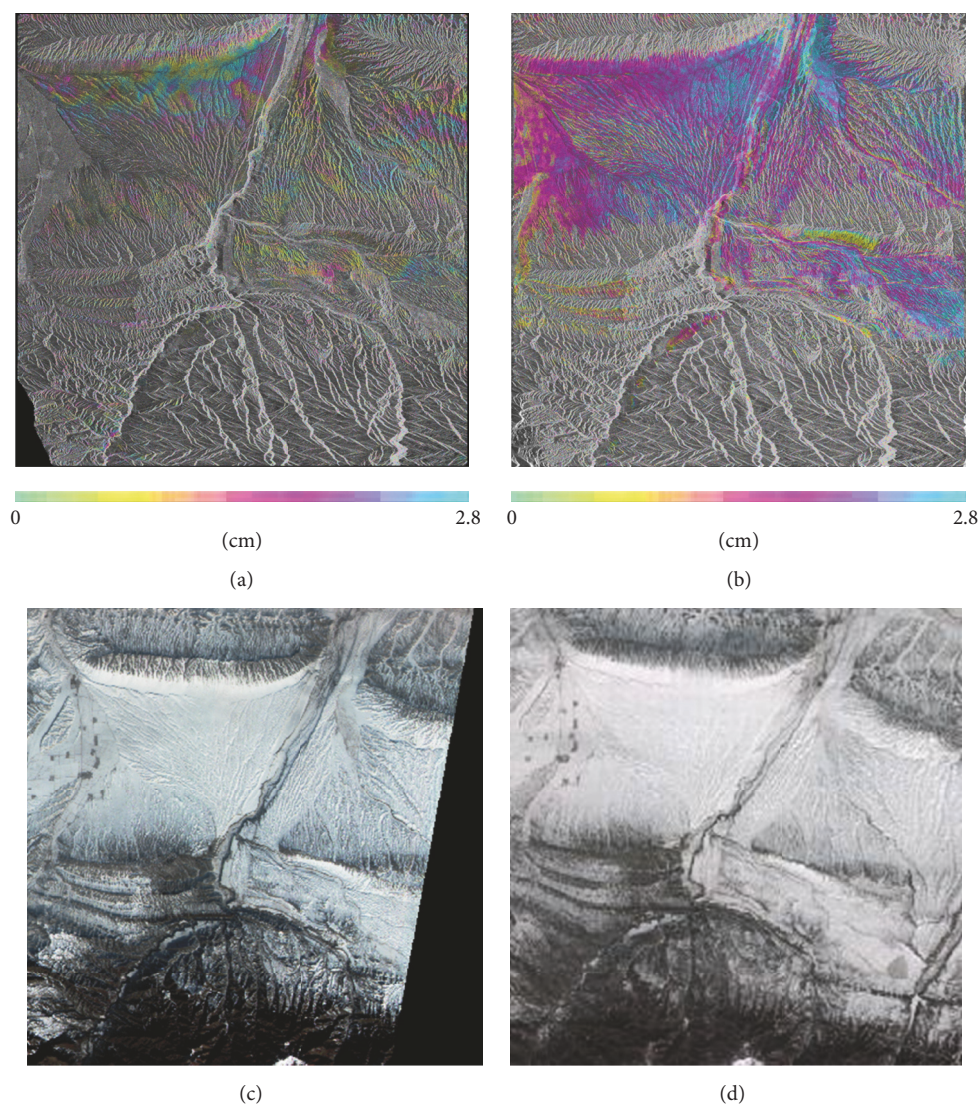


FIGURE 10: Radar-LOS displacement maps of (a) 080712-090103 and (b) 090103-090207 InSAR pairs and (c) HJ-1A CCD optical data for the study area (local time: 2009/01/03) and (d) HJ-1A CCD optical data for the study area (local time: 2009/02/09).

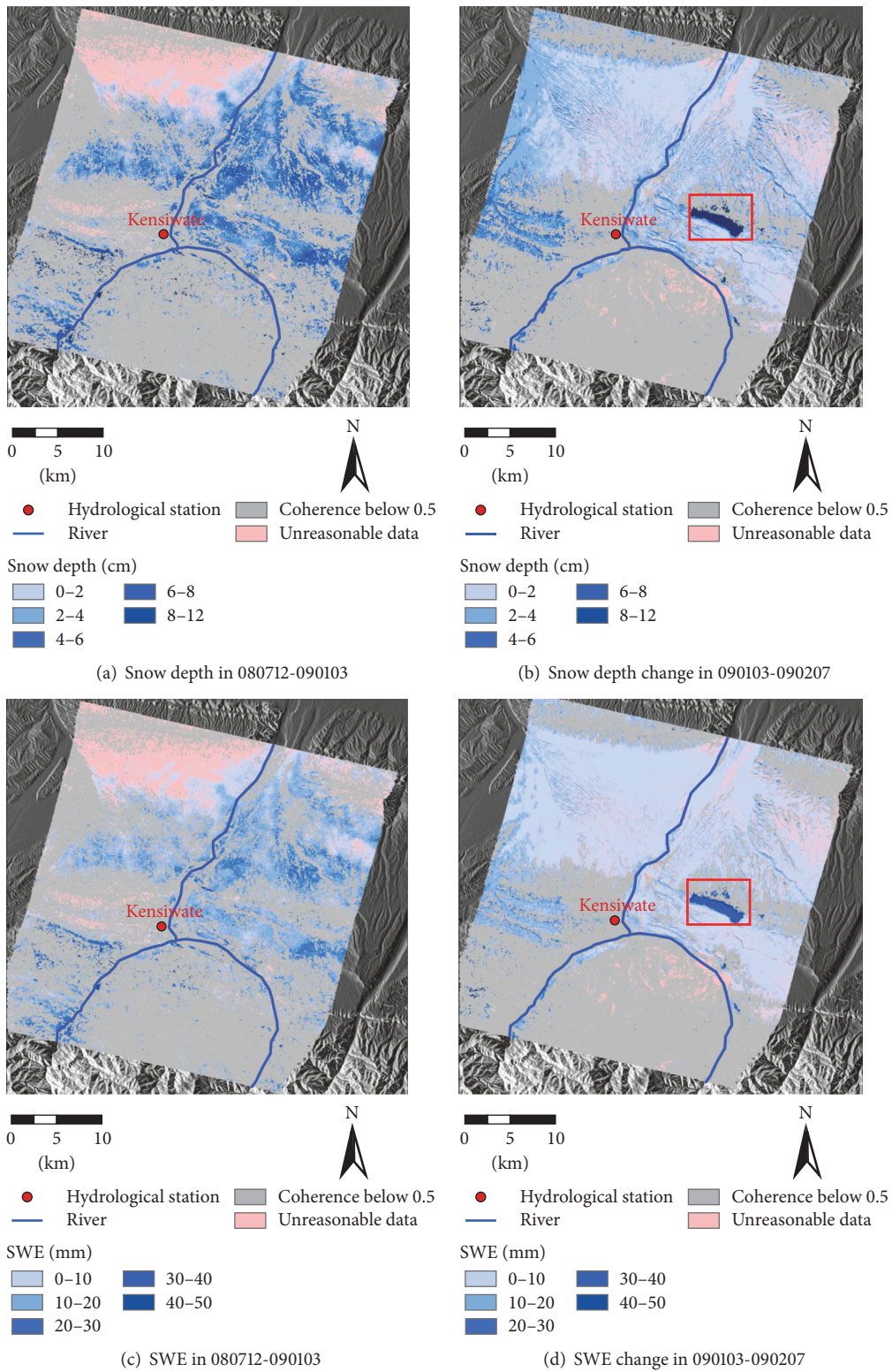


FIGURE 11: Snow depth estimation in (a) 080712-090103 InSAR pair and snow depth changes in (b) 090103-090207 InSAR pair and SWE estimation in (c) 080712-090103 InSAR pair and SWE changes in (d) 090103-090207 InSAR pair.

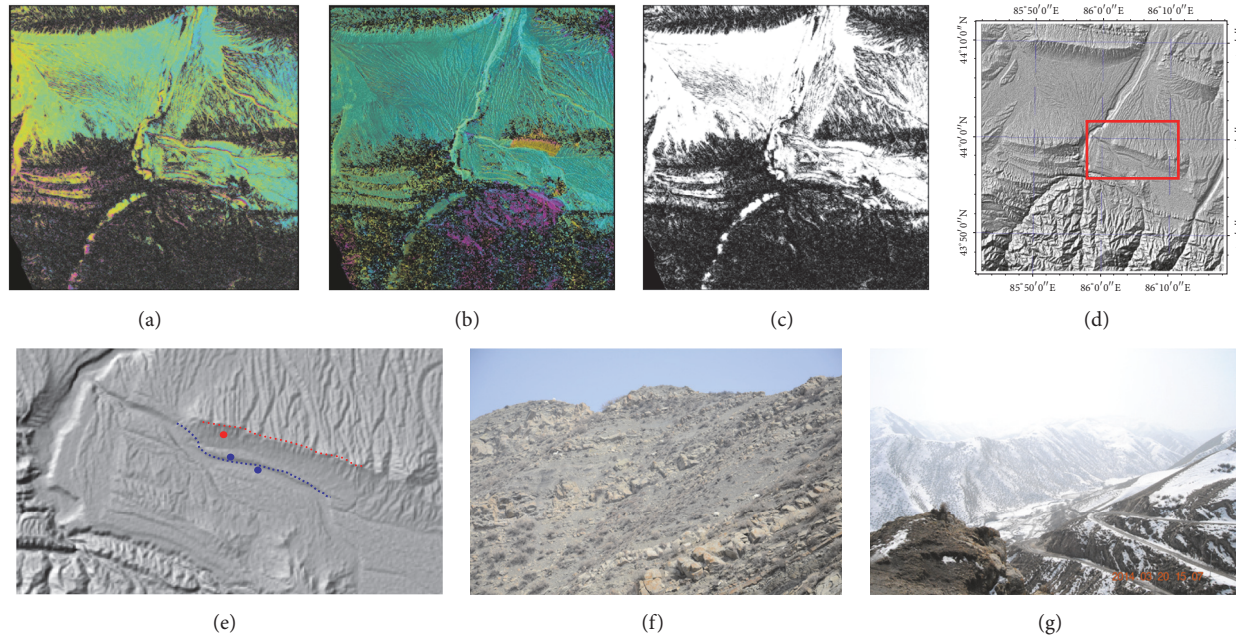


FIGURE 12: (a) The filtered differential interferogram of the 090103-090207 InSAR pair; (b) the unwrapped phase of differential interferogram by using the phase unwrapping method MCF in Gamma software; (c) the coherence image; (d) DEM image of the study area; (e) the enlarged area of the red rectangle frame in (d); ((f) and (h)) the photos in the red point in (e).

However, unreasonable estimation data existed (in pink color in Figure 11), and the pink colored area in the 080712-090103 pair was larger than in the 090103-090207 pair. As mentioned above, the atmospheric phase cannot be referred to at the time of 2008/07/12 because there was no detailed information on the atmospheric propagation conditions. In the pink colored area, the snow phase might be mixed with the atmospheric phase, and then snow depth or SWE was calculated to be under 0. Moreover, an area within the red rectangle frame (see Figures 11(b) and 11(d)) was shown in the color of dark blue to indicate a higher snow depth change of 8–12 cm and SWE change of 30–40 mm compared to the surroundings. Figure 12(a) shows the filtered differential interferogram of the 090103-090207 InSAR pair after the removal of the topographic and flattened phases, and the colored fringe was in the same pattern corresponding to the coherence image with high degree coherence (the color closer to white) (Figure 12(c)). Figure 12(b) demonstrates the unwrapped differential phase by using the phase unwrapping method MCF in Gamma software, and the black blocks were the area masked by using the coherence image below 0.25. And the phase unwrapping errors were revealed in the colors of purple and orange. As for the purple colored area, the lower coherence degree due to the rugged terrain was the main reason leading to the phase unwrapping errors. With regard to the orange colored area (see Figure 12(b)), it can be observed that sharp discontinuities in the unwrapped phase (Figure 12(a)) and coherence image (Figure 12(c)) existed along with the edges of the orange area. A rectangular area outlined in red in Figure 12(d) is enlarged to show greater detail of the pattern of DEM in Figure 12(e). In the DEM

image, the red dotted line was located along with the ridges, and the blue dotted line was located along with the deep canyon, and two small villages with farmland lied in the river valley (see the two blue points in Figure 12(e)). And there is a coincidence that the two lines accorded with the edge of discontinuities in the unwrapped phase and coherence image. Moreover, Figures 12(f) and 12(g) show the pictures we took in the position of red point in Figure 12(e) on 30 March 2014. It can be figured out that the topographic conditions are very complex and land surface patterns are diverse in this area. Therefore, even though higher coherence existed, the phase unwrapping errors occurred due to the gaps of the unwrapped phase and coherence and then resulted in a deep snow depth change and SWE change results with the dark blue color in Figures 11(b) and 11(d).

4.2. Error Sources and Propagation. High coherence indicated that the scattering properties on the ground remained relatively constant at the time of the two SAR acquisitions, and this is a desired condition for change analysis. The interferogram exhibited a clean fringe pattern, and the results for the snow depth and SWE estimation were deemed appropriate and reasonable [28]. For these two InSAR pairs, low coherence was observed in the mountainous areas of the Manas River Basin, which was mostly likely related to the rugged terrain and coniferous forest.

The total coherence is influenced by four main factors: (1) thermal or system noise, caused by the characteristics of the system and depending on the signal-to-noise ratio (for dry snow cover, the contribution to decorrelation is very small); (2) baseline or geometric decorrelation, caused

by the difference in incident angles between the two SAR acquisitions (this aspect has to be considered, because the variation of snowpack (snowfall or redistribution) in the vertical direction could change the radar geometry); (3) volume decorrelation, caused by penetration of the radar wave in the scattering medium (it has been shown to be significantly smaller than the geometric decorrelation in the C- and L-bands, even for a snowpack that is several meters deep [38]); (4) temporal decorrelation caused by physical changes in the terrain, especially for farmland and coniferous forest, affecting the scattering characteristics of the ground. This is the main reason for a decrease in the coherence of repeat-pass InSAR data over snow-covered areas. Decorrelation is not caused by a uniform snow layer, whereas the decorrelation due to snowfall and snow drift is a major problem in the C-band and has to be considered [14]. In addition, other factors such as imperfect baseline estimation (and therefore flattening) and errors or inaccuracies in the DEM may also affect the phase [28]. Moreover, accurate correction of the atmospheric phase screen in single InSAR pairs requires spatially detailed information on the atmospheric propagation conditions (in particular water vapor) which is usually not available [14]. Therefore, the errors for snow depth and SWE estimations do exist if the differences of the atmospheric phase ϕ_{atm} (see (13)) in the two SAR images are neglected and that would be the main reason of the unreasonable data in Figure 11. And, also, the process of phase unwrapping would produce an unwrapped phase jump due to the gaps in the wrapped phase and coherence where the terrain is complex and then induce the errors to the final unwrapped differential phase (snow phase).

Some other factors also result in decorrelation and may influence the results: (1) processing induced decorrelation, for example, phase unwrapping, could induce an unstable phase because of low coherence in rugged areas. The precision of the external DEM could also introduce error in the simulated topographic phase; (2) input parameters may not describe ground truth conditions accurately. A repeat orbit time (35 days or longer) is relatively long compared to the timescale of snowpack development. Depictions of snowpack can suffer from other decorrelation sources such as snow drift (wind erosion and deposition), snowfall, snow metamorphism, melting, and aging. Snow density varies vertically in homogeneously layered snow; and the propagation path of radar waves in snow is more complex in layered snowpack. In addition, differences in vertical stratification between the two SAR acquisitions can influence the interferometric phase significantly [28].

5. Conclusion and Discussion

We have presented an application for estimating snow depth and SWE for dry snow by using InSAR measurements in the Manas River Basin. A critical issue for this application is land use/cover change due to temporal decorrelation, and snow is the main reason for the deterioration of the degree of coherence of repeat-pass InSAR pairs, while a better degree of coherence was found for dry snow. The direct relationship between InSAR phase difference and SWE is the

basis for this application. A preliminary sensitivity analysis was developed, and the rates of changes of snow phase versus the incident angle and snow density were calculated. The results show that the incident angle of sensors has a crucial influence on InSAR phase and also on SWE estimation and an incident angle less than 50° does not show a significant effect on the rate of snow phase change with respect to the incident angle and snow density, but the snow phase increases exponentially for greater incident angles. Moreover, input parameters were calibrated, and the local incident angle was used as a substitute for the satellite incident angle to improve the snow depth estimation results.

For this application, snow properties of field measurements were analyzed in detail to insure that the snow was in a dry condition during the SAR acquisitions. Snow density varied between 0.16 g/cm^3 for fresh snow and 0.25 g/cm^3 for aging snow (in melting snow). All these conditions demonstrated that InSAR technology has a good potential for estimating snow depth and SWE in this area. Considering the air temperature and satellite overpass time, we ensured choosing InSAR pairs with a high degree of coherence and a small standard deviation for fine coregistration. Based on the coherence images, it was determined that geometric distortion due to rugged terrain as well as land use/cover changes due to a long temporal baseline had significant influences on decorrelation, apart from the effects of snow. A comparison of our snow depth and SWE estimation results with data from optical images showed that most of the snow-covered area was detected and had a similar pattern in the optical images. Error evaluation, atmospheric phase residual, temporal decorrelation, InSAR processing, and input parameters were discussed in earlier sections.

In this research, we assumed a uniform single layer of snowpack for snow depth estimation. However, complicated snowpack structures due to temperature gradients (relative to snow density) and roughness of snow surface at the subpixel scale (relative to local incident angle) due to snow distribution exist in the natural state, and, with limited ground truth, these conditions are difficult to identify. In future research, a complex multilayer in situ snowpack stratigraphy model should be considered to derive the snow depth and SWE changes more accurately with InSAR technology. A SAR platform with a longer wavelength (e.g., ALOS PALSAR with the L-band) should be used to estimate snow depth because this type of sensor is less affected by temporal decorrelation, has better coherence, and is capable of obtaining a larger measurement range. In this research, we have proved that InSAR measurement is a promising potential method on snow depth and SWE estimation with a higher resolution than manual sampling methods, optical and passive microwave remote sensing. However, it was a regret that limited field measurements data at the time of SAR pairs passing by can be used to validate the snow depth and SWE estimation results efficiently, but only comparisons with snow cover from optical images were processed to verify whether the results were convincing. In the following research, several field measurements with synchronous observation of Radarsat-2 satellite have been carried out in the study area, and data

analysis is in processing to improve and complete the InSAR research on snow depth and SWE estimation.

Conflicts of Interest

The authors declare that they have no conflicts of interest.

Acknowledgments

This study was funded by the National Natural Science Foundation of China (NSFC) (Grants nos. 41401377 and 41501379), the Natural Science Foundation of Fujian Province (Grant no. 2015J01175), and the Education and Scientific Research Project (Type A) for Young and Middle-Aged Teachers of Fujian Province (no. JA14231) and was also conducted as part of the PPP Project (Project Based Personnel Exchange Program) with China Scholarship Council (CSC) and the German Academic Exchange Service (DAAD). Thanks are due to ESA for the provision of ASAR data in the framework of the Dragon 2 Program (Project ID 5322, Key Ecohydrological Parameters Retrieval and Land Data Assimilation System Development in a Typical Inland River Basin of China's Arid Region). Thanks are due to Professor Lorenz King, Dr. Eliso, and Stephan Imbery from the Geographical Institute, Justus Liebig University Giessen, Germany, for they gave valuable suggestions and provided information of snow and glacier in Tianshan Mountains.

References

- [1] J. C. Shi, "Active microwave remote sensing systems and applications to snow monitoring," in *Advances in Land Remote Sensing: System, Modelling, Inversion and Application*, S. L. Liang, Ed., Springer, Berlin, Germany, 2008.
- [2] A. Rango, J. Martinec, A. T. C. Chang, J. L. Foster, and V. van Katwijk, "Average areal water equivalent of snow in a mountain basin using microwave and visible satellite data," *IEEE Transactions on Geoscience and Remote Sensing*, vol. 27, no. 6, pp. 740–745, 1989.
- [3] A. W. Nolin, "Recent advances in remote sensing of seasonal snow," *Journal of Glaciology*, vol. 56, no. 200, pp. 1141–1150, 2011.
- [4] D. Robinson, K. Kunzi, G. Kukla, and H. Rott, "Comparative utility of microwave and shortwave satellite data for all-weather charting of snow cover," *Nature*, vol. 312, no. 5993, pp. 434–435, 1984.
- [5] L. Jiang, J. Shi, S. Tjuatja, K. S. Chen, J. Du, and L. Zhang, "Estimation of snow water equivalence using the polarimetric scanning radiometer from the cold land processes experiments (CLPX03)," *IEEE Geoscience and Remote Sensing Letters*, vol. 8, no. 2, pp. 359–363, 2011.
- [6] R. Storvold, E. Malnes, Y. Larsen et al., "SAR remote sensing of snow parameters in norwegian areas—current status and future perspective," *Journal of Electromagnetic Waves and Applications*, vol. 20, no. 13, pp. 1751–1759, 2006.
- [7] J. Shi and J. Dozier, "Estimation of snow water equivalence using SIR-C/X-SAR, Part I: inferring snow density and subsurface properties," *IEEE Transactions on Geoscience and Remote Sensing*, vol. 38, no. 6, pp. 2465–2474, 2000.
- [8] J. Shi and J. Dozier, "Estimation of snow water equivalence using SIR-C/X-SAR, Part II: inferring snow depth and particle size," *IEEE Transactions on Geoscience and Remote Sensing*, vol. 38, no. 6, pp. 2475–2488, 2000.
- [9] D. Massonnet, P. Briole, and A. Arnaud, "Deflation of Mount Etna monitored by spaceborne radar interferometry," *Nature*, vol. 375, no. 6532, pp. 567–570, 1995.
- [10] G. Luzi, M. Pieraccini, D. Mecatti et al., "Ground-based radar interferometry for landslides monitoring: atmospheric and instrumental decorrelation sources on experimental data," *IEEE Transactions on Geoscience and Remote Sensing*, vol. 42, no. 11, pp. 2454–2466, 2004.
- [11] R. M. Goldstein, H. Engelhardt, B. Kamb, and R. M. Frolich, "Satellite radar interferometry for monitoring ice sheet motion: application to an Antarctic ice stream," *Science*, vol. 262, no. 5139, pp. 1525–1530, 1993.
- [12] J. Shi, S. Hensley, and J. Dozier, "Mapping snow cover with repeat pass synthetic aperture radar," in *Proceedings of the IEEE International Geoscience and Remote Sensing Symposium (IGARSS '97)*, pp. 628–630, August 1997.
- [13] T. Guneriusson, K. A. Høgda, H. Johnsen, and I. Lauknes, "InSAR for estimation of changes in snow water equivalent of dry snow," *IEEE Transactions on Geoscience and Remote Sensing*, vol. 39, no. 10, pp. 2101–2108, 2001.
- [14] H. Rott, "Snow mass retrieval by means of SAR interferometer," in *Proceedings of FRINGE 2003 Workshop, Frascati, Italy*, 2004.
- [15] E. J. Deeb, R. R. Forster, and D. L. Kane, "Monitoring snowpack evolution using interferometric synthetic aperture radar on the north slope of Alaska, USA," *International Journal of Remote Sensing*, vol. 32, no. 14, pp. 3985–4003, 2011.
- [16] V. Kumar and G. Venkataraman, "SAR interferometric coherence analysis for snow cover mapping in the western Himalayan region," *International Journal of Digital Earth*, vol. 4, no. 1, pp. 78–90, 2011.
- [17] G. Luzi, "Ground based SAR interferometry: a novel tool for geoscience," in *Geoscience and Remote Sensing New Achievements*, chapter 1, pp. 1–26, InTech, Rijeka, Croatia, 2010.
- [18] H. Rott, K. Sturm, and H. Miller, "Active and passive microwave signatures of Antarctic firn by means of field measurements and satellite data," *Annals of Glaciology*, vol. 17, pp. 337–343, 1993.
- [19] E. Rignot, K. Echelmeyer, and W. Krabill, "Penetration depth of interferometric synthetic-aperture radar signals in snow and ice," *Geophysical Research Letters*, vol. 28, no. 18, pp. 3501–3504, 2001.
- [20] C. Mätzler, "Microwave permittivity of dry snow," *IEEE Transactions on Geoscience and Remote Sensing*, vol. 34, no. 2, pp. 573–581, 1996.
- [21] R. F. Hanssen, *Radar Interferometry: Data Interpretation and Error Analysis*, Kluwer Academic Publishers, Dordrecht, The Netherlands, 2001.
- [22] G. Engen, T. Guneriusson, and Ø. Overrein, "Delta-K interferometric SAR technique for snow water equivalent (SWE) retrieval," *IEEE Geoscience and Remote Sensing Letters*, vol. 1, no. 2, pp. 57–61, 2004.
- [23] M. Durand, E. J. Kim, and S. A. Margulis, "Quantifying uncertainty in modeling snow microwave radiance for a mountain snowpack at the point-scale, including stratigraphic effects," *IEEE Transactions on Geoscience and Remote Sensing*, vol. 46, no. 6, pp. 1753–1767, 2008.
- [24] T.-D. Wu, K. S. Chen, J. Shi, and A. K. Fung, "A transition model for the reflection coefficient in surface scattering," *IEEE Transactions on Geoscience and Remote Sensing*, vol. 39, no. 9, pp. 2040–2050, 2001.

- [25] A. Wiesmann and C. Mätzler, "Microwave emission model of layered snowpacks," *Remote Sensing of Environment*, vol. 70, no. 3, pp. 307–316, 1999.
- [26] L. Dai, T. Che, J. Wang, and P. Zhang, "Snow depth and snow water equivalent estimation from AMSR-E data based on a priori snow characteristics in Xinjiang, China," *Remote Sensing of Environment*, vol. 127, pp. 14–29, 2012.
- [27] X. Z. Feng, W. J. Li, Z. T. Shi, and L. H. Wang, "Satellite Snowcover monitoring and snowmelt runoff simulation of Manas river in Tianshan region," *Remote Sensing Technology and Application*, vol. 15, no. 1, pp. 18–21, 2000.
- [28] H. Li, P. Xiao, X. Feng, G. He, and Z. Wang, "Monitoring snow depth and its change using repeat-pass interferometric SAR in Manas River Basin," in *Proceedings of the IEEE International Geoscience and Remote Sensing Symposium (IGARSS '16)*, Beijing, China, July 2016.
- [29] R. J. Hu, *Physical Geography of the Tianshan Mountains in China*, China Environmental Science Press, Beijing, China, 2004.
- [30] P. A. Rosen, S. Hensley, I. R. Joughin et al., "Synthetic aperture radar interferometry," *Proceedings of the IEEE*, vol. 88, no. 3, pp. 333–380, 2000.
- [31] A. Esmaily-Gazkohani, H. B. Granberg, and Q. H. J. Gwyn, "Repeat-pass cross-track interferometric SAR to measure dry snow water equivalent and depth," *Canadian Journal of Remote Sensing*, vol. 36, no. 2, pp. S316–S326, 2010.
- [32] K. E. Mattar, A. L. Gray, D. Geudtner, and P. W. Vachon, "Interferometry for DEM and terrain displacement: effects of inhomogeneous propagation," *Canadian Journal of Remote Sensing*, vol. 25, no. 1, pp. 60–69, 1999.
- [33] K. Sarabandi, " Δk -radar equivalent of interferometric SARs: a theoretical study for determination of vegetation height," *IEEE Transactions on Geoscience and Remote Sensing*, vol. 35, no. 5, pp. 1267–1276, 1997.
- [34] F. Domine, M. Albert, T. Huthwelker et al., "Snow physics as relevant to snow photochemistry," *Atmospheric Chemistry and Physics*, vol. 8, no. 2, pp. 171–208, 2008.
- [35] T. Strozzi, U. Wegmüller, and C. Mätzler, "Mapping wet snowcovers with SAR interferometry," *International Journal of Remote Sensing*, vol. 20, no. 12, pp. 2395–2403, 1999.
- [36] C. Sun, C. M. U. Neale, and J. J. McDonnell, "Snow wetness estimates of vegetated terrain from satellite passive microwave data," *Hydrological Processes*, vol. 10, no. 12, pp. 1619–1628, 1996.
- [37] F. Chen, H. Lin, W. Zhou, T. Hong, and G. Wang, "Surface deformation detected by ALOS PALSAR small baseline SAR interferometry over permafrost environment of Beiluhe section, Tibet Plateau, China," *Remote Sensing of Environment*, vol. 138, pp. 10–18, 2013.
- [38] E. Weber Hoen and H. A. Zebker, "Penetration depths inferred from interferometric volume decorrelation observed over the Greenland ice sheet," *IEEE Transactions on Geoscience and Remote Sensing*, vol. 38, no. 6, pp. 2571–2583, 2000.



Hindawi

Submit your manuscripts at
<https://www.hindawi.com>

